Coastal-Trapped Waves on the West Coast of South Island, New Zealand

MADELEINE L. CAHILL AND JASON H. MIDDLETON

School of Mathematics, University of New South Wales, Kensington, NSW, Australia

BASIL R. STANTON

New Zealand Oceanographic Institute, Kilbirnie, Wellington, New Zealand

(Manuscript received 14 March 1990, in final form 22 October 1990)

ABSTRACT

The coastal ocean response to wind forcing on the west coast continental shelf of South Island, New Zealand is examined using current, sea level and wind observations. Weather band motions over the northern region of the shelf appear to be dominated by the response to wind-forced flux through Cook Strait. Through-strait forcing is still evident in the currents of the southern region but west coast alongshore wind-forcing is also important.

Most of the variance of nearshore weather band currents in the northern region of the shelf can be described in terms of coastal-trapped waves (CTWs). A fit of CTW modes 1 and 2 to the observations in that region indicates the equal importance of both modes, in agreement with the theories of strait-generated CTWs. Farther south, the across-shelf depth profile alters dramatically such that CTW structures change from being almost barotropic in the northern region to highly baroclinic. This rapid change in topography suggests that considerable scattering of CTWs might occur, a hypothesis which is supported by current observations in the southern region of the shelf.

1. Introduction

The importance of a wide strait as a possible source for coastal-trapped waves (CTWs) was suggested by Crawford and Thomson (1984) and Crawford (1984) who observed diurnal period CTWs propagating northward along the coast of Vancouver Island from Juan de Fuca Strait. Flather (1988) reproduced this observation in a numerical model of the region and showed that by blocking the strait to through-flow the CTWs in the model disappeared. Similarly, in the analysis of data from the Australian Coastal Experiment (ACE) on the southeast coast of Australia, Church et al. (1986a,b) and Freeland et al. (1986) found that much of the weather band energy on the shelf (once the East Australian Current signal was removed from the data) was due to free CTW modes 1 and 2 which appeared to have been generated in Bass Strait. Buchwald and Kachoyan (1987, hereafter BK) subsequently reproduced this result analytically for an unstratified ocean, showing that an oscillating coastal flux could generate free shelf waves, the amplitude of each mode being determined by the ratio of the width of the strait to the CTW wavelength. In particular, for the ACE region BK's theory predicted the large mode 2 response that was observed.

Cook Strait, separating North and South Island of New Zealand by 140 km on the western side (Fig. 1), might be anticipated to be analogous to Bass Strait with regard to the generation of CTWs. Indeed, the theory of BK predicts that coastal velocity amplitudes associated with CTW modes 1 and 2 are nearly equal on the west coast South Island shelf, being downstream (in the sense of CTW propagation) from Cook Strait. In this paper we analyze data from the first long term deployment of moored current meters on this shelf and investigate the prediction of BK.

This paper is organized as follows. In section 2, the field program and other available data are described. Then in section 3 we present a preliminary analysis (largely in the frequency domain) of the current meter and wind data. In the next two sections, dynamic modes are fitted to the current data and the results are compared with BK's theory of CTW generation by a coastal flux. In section 6, a simple comparison is made between the CTWs observed in the northern region of the shelf and currents recorded farther south. We conclude with a discussion of the results and their relationship to the observations of ACE.

2. Data acquisition and preparation

The current meter and pressure gauge array was deployed in November 1986 and recovered in April 1987 as part of the NZOI West Coast Ecosystem Programme. The deployed array comprised 14 current meters and

Corresponding author address: Madeleine Cahill, University of New South Wales, School of Mathematics, Kensington, New South Wales, 2033 Australia.

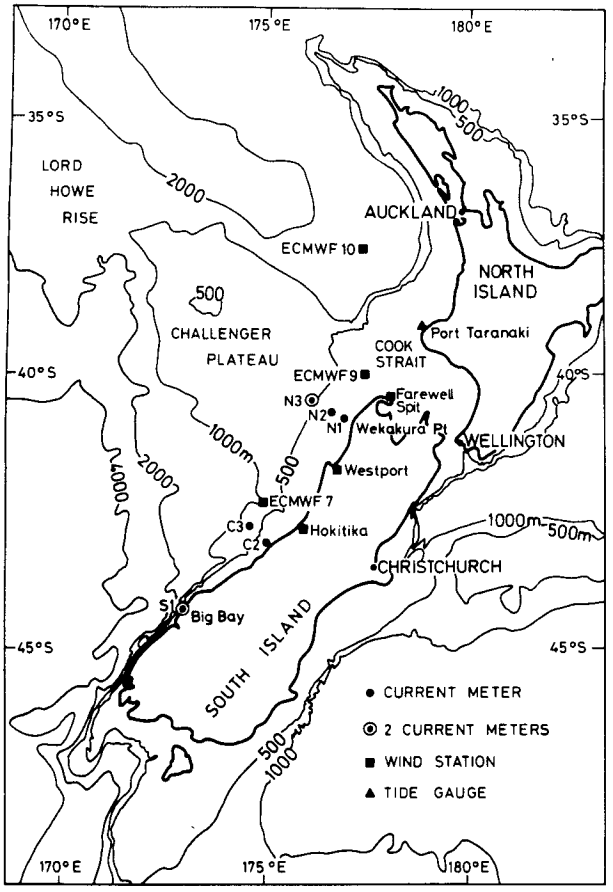

FIG. 1. Topographic map of New Zealand waters showing recording instrument locations.

three pressure gauges but due to heavy losses, largely caused by trawlers, there is data from only eight current meters and there is no pressure gauge data. Of particular note is the loss of moorings from Cook Strait (off Wellington) and the North Island shelf (off Port Taranaki). The absence of data from these moorings creates uncertainty in some aspects of the analysis and interpretation.

The recovered array, as shown in Fig. 1, includes a line of four current meters on three moorings perpendicular to the coast at Wekakura Point (41°S, 172°E) just 70 km south of Cook Strait, and one dual-meter mooring 520 km southwest along the coast at Big Bay (44°16′S). Of the intermediate current meter line deployed at 43°S, data (of length > 35 days) exists from only one current meter at 750 m depth in 800 m of water. All current meters were Aanderaa RCM4s, recording temperature as well as speed and direction at hourly intervals. In this paper the mooring lines are referred to as Northern, Central and Southern. Each instrument is referred to first by its line (either N, C or S), then the mooring number, mooring 1 being closest to the coast. If there were two meters on the mooring, a T or B is used to indicate top or bottom. Mooring and instrument depths are shown in Table 1.

The topography of the west coast shelf of New Zealand is complicated by the presence of Lord Howe Rise. This wide ridge runs perpendicular to the coast of New Zealand from the northern region of South Island, where it is called the Challenger Plateau, to halfway across the Tasman Sea. In the region of the rise, the depth transition from the coast to Challenger Plateau is gradual (average gradient of 1 in 200) and the plateau then extends 400 km farther seawards at a depth of only 750 m. Northeast and southwest of the rise the shelf margin narrows and steepens, particularly in the south where depths of 4000 m are attained within 20 km of the coast. The northern line of current meters was deployed just south of Cook Strait in the region of Lord Howe Rise and S1 was deployed 520 km south where the shelf is very narrow.

Hydrographic observations were made along six lines perpendicular to the coast between 41° and 44°S during both the deployment and recovery cruises using a

TABLE 1. Statistics of the low-pass filtered data from the moored current meter and wind station records: mooring number or wind station name, depth of water (m), instrument depth (m), record length, amplitude and direction of the mean (cm s^{-1}, °T or N m^{-2} for windstress), orientation of the principal axis (°T), standard deviation of the velocity and windstress along the principal axis (sV) and orthogonal to it (sU).

Instrument site	Water depth	Meter depth	Mean amp.	Mean dir.	Length (days)	Principal axis	sV	sU
N1	74	47	0.8	82	172	25	11.6	1.8
N2	140	70	4.7	73	170	40	7.7	4.0
N3T	550	100	3.4	174	171	20	6.5	4.4
N3B	550	500	0.4	212	171	30	1.9	1.6
C2	200	170	3.7	233	29	50	4.9	2.1
C3	800	750	1.5	239	170	15	3.0	2.6
S1T	77	55	4.9	210	169	35	7.9	1.7
S1B	77	66	3.6	211	169	40	5.0	1.3
Farewell spit	—	—	0.030	130	210	120	0.070	0.046
Hokitika	—	—	0.008	148	210	45	0.028	0.015
Westport	—	—	0.012	77	210	45	0.037	0.019
ECMWF9	—	—	0.043	105	210	120	0.090	0.078
ECMWF7	—	—	0.022	112	210	30	0.052	0.048

Guildline Conductivity, Temperature and Depth (CTD) probe. Along each line stations were about 20 km apart, closer together nearshore, and were continued to ~200 km from shore. Each cruise was of three weeks duration, and the CTD profiles were carried out almost continuously during that time so most sections were profiled at least twice.

Wind speed and direction, recorded at 3-hour intervals, were obtained for the duration of the deployment from three coastal stations: Farewell Spit in Cook Strait and Westport and Hokitika along the west coast (Fig. 1). The wind velocities measured at Farewell Spit are believed to be representative of winds through Cook Strait because the narrow spit extends almost 10 km into the strait and has little elevation. However, the wind stations on the west coast are backed by the Southern Alps and hence may not give an accurate measure of winds over the shelf waters. Geostrophically determined winds from the European Centre for Medium Range Weather Forecasting (ECMWF) were obtained at every 2.5° of latitude and longitude along the west coast at locations nearby the coastal stations. Wind measurements were also taken using the ship's anemometer at each CTD station during the deployment and recovery cruises for further verification of winds over the shelf waters. An initial analysis of this data indicates that the geostrophic winds are representative of the wind over the ocean to within at least 30 km from the coast. Wind stress estimates were calculated from the three-hourly velocity data using the neutral, steady-state expression of Large and Pond (1981).

The only representative sea level data available for the duration of the field study were obtained from the harbour tide gauge at Port Taranaki on North Island (39°S). The sea level data were digitized at hourly intervals and corrected for the barometric response to simulate bottom pressure.

All current, sea level and wind data presented here are low-pass filtered, using a Fourier transform filter tapered over 10% of the passed coefficients, such that the half-power point is at 0.6 cpd (cycles per day). The filtered timeseries are subsampled at 12-hour intervals.

3. Preliminary observations

a. Hydrographic observations

CTD profiles taken during November 1986 and April 1987 show a sharp pycnocline, due largely to the temperature gradient, about 60 m below the surface. For the duration of each cruise the hydrographic profiles did not vary qualitatively either along or across the shelf. Between cruises, however, the strength of the stratification increased at the base of the mixed layer. The profiles shown in Fig. 2, from 150 km offshore in 750 m of water in November (ship station v011) and 950 m in April (ship station v167), are taken to be representative of conditions at the shelf edge during each cruise. Broadly speaking, in April the surface mixed layer is ~20 m deeper, ~1°C warmer and 0.1 psu less saline than in November, leading to a higher maximum N in April. Below the mixed layer, however, the profile of N appears to have remained substantially constant during the deployment. In terms of their effect on theoretical CTW properties, the two profiles are found to be almost the same.

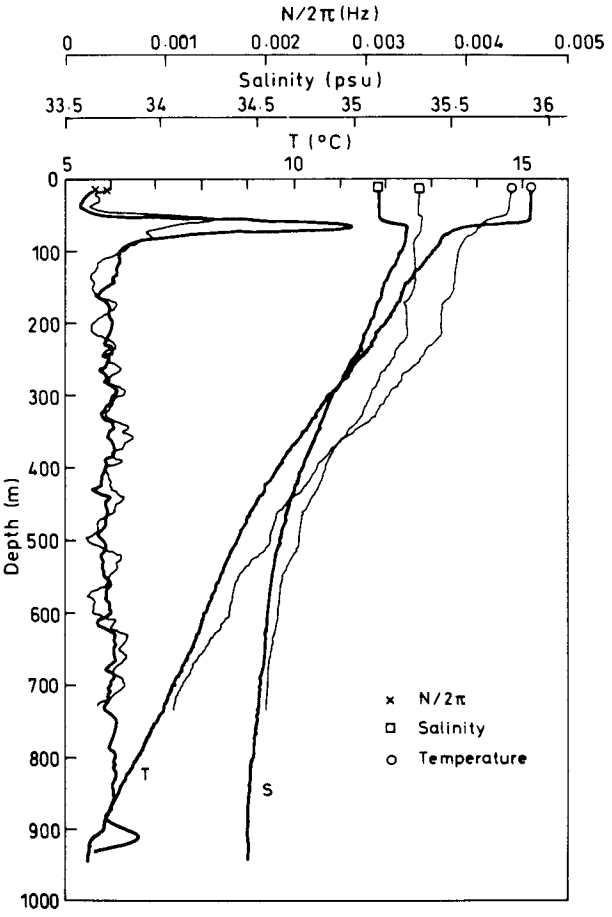

FIG. 2. Profiles of Brunt–Väisälä frequency, salinity and temperature for the November (thin line) and April (thick line) cruises.

b. Currents

Time series of low-pass filtered currents (Fig. 3) show that maximum velocities are found inshore on the northern line at N1, where observed speeds reach 30 cm s^{-1} although the mean flow is negligible. Currents measured at the southern mooring at a corresponding depth are not as strong, and have a southwestward mean. At both of these inshore moorings currents are rectilinear while farther offshore, on the northern line at N2, the current vectors are more rotational with the anticlockwise rotary autospectral components (not shown) being twice as energetic as the clockwise components. At the outer mooring N3, 95 km from the

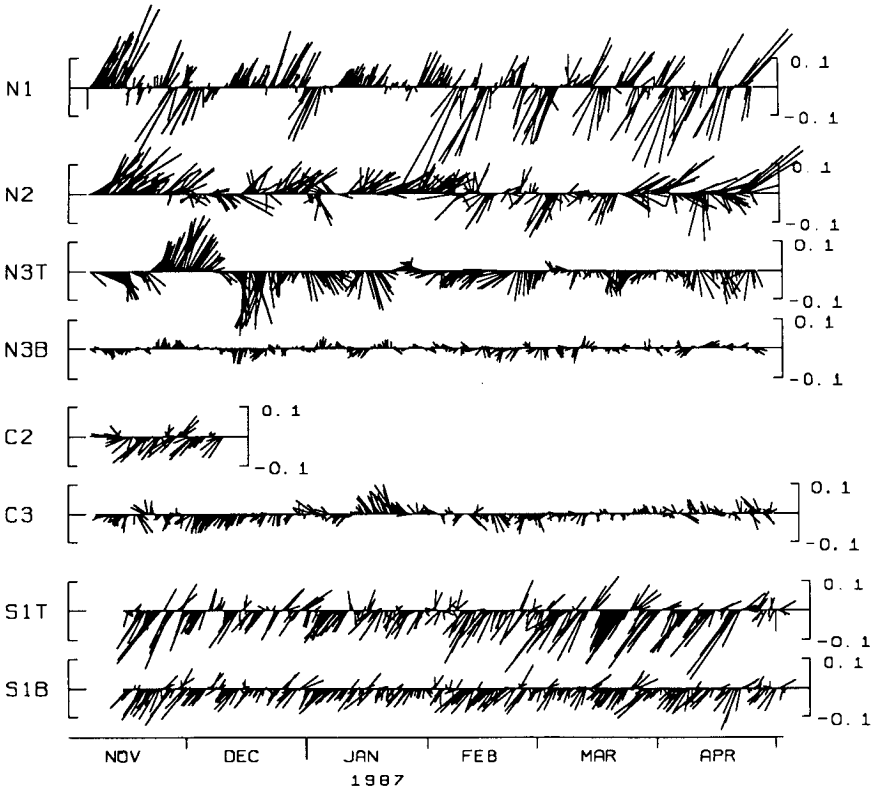

FIG. 3. Time series of low-pass filtered current vectors from all meters. A northward current is drawn as a vector pointing to the top of the page. Units are m s^{-1}.

coast, currents are weak ($\sim$5 cm s^{-1}) at 500 m depth (N3B) while maximum speeds of 20 cm s^{-1} were recorded at the top meter (N3T) at 100 m depth. The strength, surface intensification, low frequency and lack of preferred direction of the current velocities at N3T in November and December suggest the predominance of eddy phenomena at this location. Table 1 shows details of all current meter and wind time series, including, for each location, the mean, standard deviations and the direction of the principal axis of variability. The alongshore direction of currents at each location is chosen to be in the direction of the most energetic mode determined by a time domain vector empirical orthogonal function (EOF) analysis (Hardy and Walton 1978). These directions correspond closely with the major axes of the current ellipses and the orientation of the local topography.

The unsmoothed autospectra (Fig. 4) of the currents at the two outer moorings (N3 and C3) are quite different to those of the currents at the other moorings. They are dominated by energy at low frequencies ($\omega < 0.05$ cpd) and have little energy at weather band frequencies ($0.05 < \omega < 0.18$ cpd, periods of 6–20 d) where the upper-shelf time series are most energetic. Coherence estimates (not shown) between currents at N3 and C3 are well below the 95% significance level except at frequencies below 0.05 cpd.

Here, and for the rest of this paper, coherence estimates referred to are those obtained by band averaging spectral and cross-spectral estimates using the Tukey window $[\frac{1}{2}(1 + \cos x)]$ with a half-amplitude width of five spectral estimates. The 95% significance level for the coherence squared (γ^2) then corresponds to a value of 0.53 (Thompson 1979). In this paper, a "significant" coherence is one which exceeds the 95% level of significance. We also define here $\mathbf{H}_{A/B}(\omega)$, the complex frequency transfer function,

$$\mathbf{H}_{A/B}(\omega) = \frac{\langle \mathrm{B}^*(\omega)\mathrm{A}(\omega)\rangle}{\langle \mathrm{B}^*(\omega)\mathrm{B}(\omega)\rangle}. \qquad (1)$$

The product in the angle brackets is averaged as above, $\mathrm{A}(\omega)$ and $\mathrm{B}(\omega)$ are the Fourier coefficients of time series $A(t)$ and $B(t)$ at frequency ω and complex conjugation is denoted by $*$. The amplitude of $\mathbf{H}_{A/B}$ is an estimate of the cospectral gain of A/B and $\theta^c_{A/B} = \arg(\mathbf{H}_{A/B})$ is an estimate of the cospectral phase difference between A and B.

The three vertical lines through the spectra of Fig. 4 indicate the centers of the frequency bands which are most energetic and coherent throughout the dataset. The two lines drawn at $\omega_1 = 0.055$ cpd and $\omega_3 = 0.13$ cpd correspond to the most energetic peaks (within the weather band) in the N1 and N2 spectra. At these two frequencies there are corresponding spectral peaks in

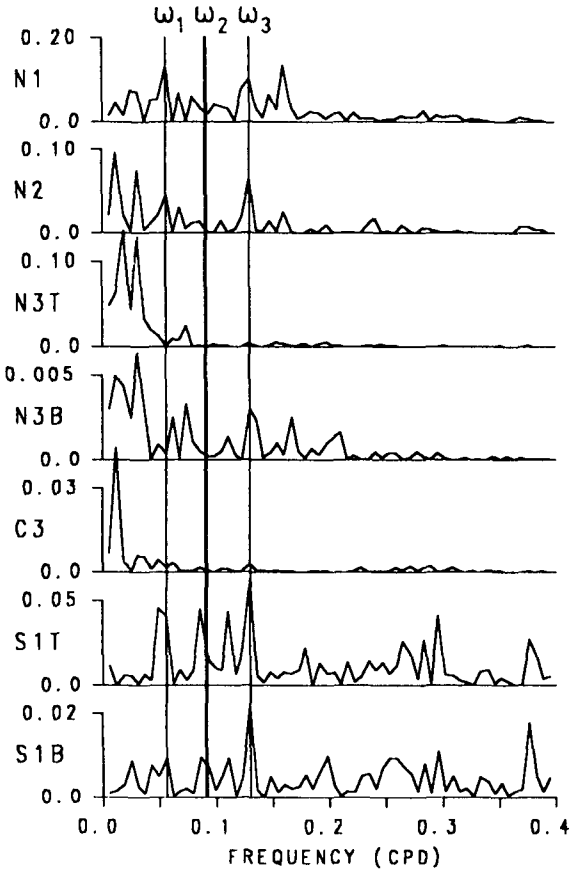

FIG. 4. Unsmoothed energy-preserving autospectra of the alongshore current component. The same number of records (161 days) were used for the Fourier transform of each time series. The significance of ω_1, ω_2 and ω_3 is explained in the text. Units are $m^2\ s^{-1}$. Note the differing scales.

the S1T and S1B spectra and also high coherence ($\gamma^2 = 0.7$, see Fig. 5a) between the northern and southern time series. A third, thicker line is drawn at $\omega_2 = 0.09$ cpd, where an energy peak at S1 is comparable with the energy at the other two frequency bands. Although there is high coherence between N1 and S1 in this frequency band, there is not a distinct peak in the spectra at either N1 or N2.

Coherence-squared estimates between alongshore currents at N1 and N2 (Fig. 5b), separated by 30 km across the shelf, are high, nearly 0.9 at almost all weather band frequencies. The currents at the inshore mooring N1 lead those at N2 at all weather band frequencies, the cospectral phase $\theta^c_{N2/N1}$ being 29 ± 7° at ω_1 decreasing linearly to 21 ± 7° at ω_3. The error estimates for phase are the 68% confidence intervals, based on coherence estimates [Bendat and Piersol 1980, Eq. (11.62)]. We shall discuss this cross-shelf phase difference in the alongshore currents in section 5.

The current at N1 is also highly coherent (Fig. 5a) with that at S1T (520 km to the south). Cospectral phase estimates $\theta^c_{S1T/N1}$ at ω_1, ω_2, and ω_3 (periods 18 d, 11 d, 7.7 d) are 56 ± 12°, 101 ± 13° and 80 ± 13°, corresponding to time lags of 3 d at ω_1 and ω_2, and 2 d at ω_3, with N1 leading.

Time series of the alongshore currents at N1, N2 and S1T are shown in Fig. 6. There is a clear visual correlation between currents at the northern and southern moorings for the latter two months of the deployment, when most of the oscillations contributing to the energy peak at ω_3 occurred. The alongshore currents are found to be maximally correlated when high frequency fluctuations at periods of a few days as well as the very long period (greater than 25 d) fluctuations are filtered from the time series. The squared correlation coefficient R^2 between the band-pass (6–25 d) filtered currents at S1T and N1 (N2) is then 0.52 (0.56) when S1T is advanced by 2.0 (1.5) d. These values of R^2 are well above the 95% significance level of 0.08. There is less visual correlation between the two time series during the earlier months of the deployment. When the data from the last two months are excluded from the correlation, R^2 between S1T and N1 (N2) is reduced to 0.28 (0.43), the lag of S1T behind N1 (N2) being 2.5 (1.5) d. The correlations are still significant for this shortened time series as the 95% significance level of R^2 is 0.12. This change with time of the correlation coefficient between currents in the north and south will be discussed further in section 3d with regard to the observed winds. Note that the different lags obtained for N1 and N2 reflects the cross-shelf phase difference in the currents at the northern line that was mentioned above.

The 95% significance level of R^2 was calculated on the assumption that a degree of freedom is obtained for every 3 d of data. This estimate represents an average of the integral time scales for the low-pass (periods longer than 6 d) filtered winds and alongshore currents. The autocorrelation function of the through-strait wind and currents at N2 passes through zero at 8.5 d lag with the integral time scale being 4.0 d. For the west coast alongshore wind and currents at N1 and S1T, the zero crossing is at 3.0 d lag and the integral time scale estimate is 2.0 d.

The two current meters on the southern mooring, S1T and S1B, are separated by only 11 m so it is hardly surprising that they are highly coherent at all frequencies above 0.03 cpd. The currents at the top meter, however, lag those at the lower meter by ~20° and the cospectral gain $|H_{S1B/S1T}|$ is ~0.5 within the weather band due, presumably, to the effects of the frictional bottom boundary layer.

The relationships between the measured currents can be most concisely described using frequency domain EOFs (see Wallace and Dickinson 1972). The analysis was performed over the three frequency bands ω_1, ω_2 and ω_3, using only the alongshore component of the velocity data from the seven current meters. The coherence squared estimates between the alongshore currents at each location and the first EOF in each fre-

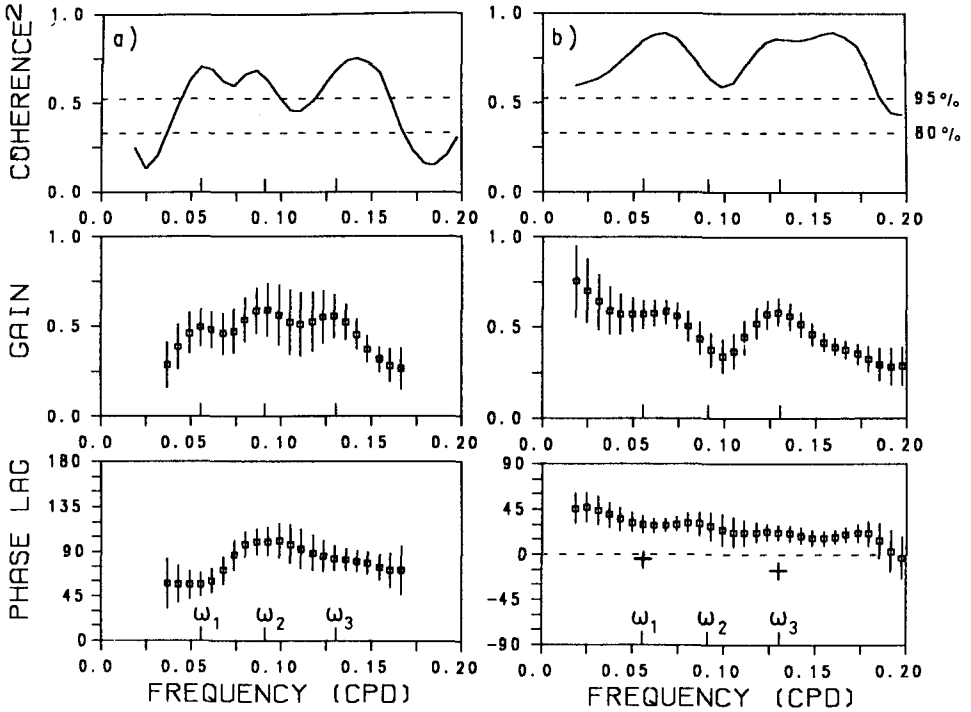

FIG. 5. Estimates of the coherence squared, cospectral gain (first series over the second) and cospectral phase between the alongshore velocities at (a) S1T and N1 and (b) N2 and N1. Values of $\theta^{l}_{N2/N1}$ (see section 5b) at ω_1 and ω_3 are plotted in (b) as +'s. A positive phase lag indicates that the first series lags the second. Phase and gain estimates are only plotted when the coherence squared is greater than the 80% significance level and only every fifth estimate shown is independent. Error bars (68%) are determined from coherence (Bendat and Piersol 1980).

quency band are given in Table 2. The first EOF is largely representative of the nearshore currents (at N1, N2, S1T and S1B) for which the average value of the coherence squared between currents at each location with the first EOF is 0.83. Currents at the outer moorings, however, are incoherent with the first EOF and therefore also with the nearshore currents, except at ω_3.

c. *Windstress*

Low-passed windstress vectors (Fig. 7) show that winds through Cook Strait are stronger than the west coast winds, with stresses of more than 0.2 N m^{-2}, according to both measurements at Farewell Spit and geostrophic winds from ECMWF9. The through-strait component of the ECMWF9 and Farewell Spit winds are significantly coherent at frequencies less than 0.2 cpd with maximum coherence at ω_1 and ω_3 ($\gamma^2 = 0.88$).

The winds measured at the coastal stations on the west coast, Westport and Hokitika, are weak, with few peak stresses greater than 0.1 N m^{-2}. The time series from Westport and Hokitika, separated by 125 km, are significantly coherent at all frequencies between 0.05 and 0.15 cpd. The maximum γ^2 (0.91) between these two west coast winds occurs at ω_2, the frequency at which only S1T and S1B (of the currents) have spectral peaks. The alongshore component of the winds from the nearest geostrophic wind station ECMWF7 is also significantly coherent in the weather band (maximally at ω_2, $\gamma^2 > 0.80$) with Hokitika and Westport alongshore winds. So it seems that at frequencies between 0.05 and 0.15 cpd all these winds are fairly representative of the wind along the west coast, although the strength of the wind forcing over the shelf waters probably lies somewhere between the measured coastal winds and the stronger geostrophic winds from ECMWF7 (75 km from the coast). Cospectral phase estimates indicate that the west coast wind propagates with an apparent phase speed of 6 m s^{-1} northeastwards along the coast, in the opposite direction to free CTWs.

The coherence between the alongshore components of the geostrophic winds over the North Island (ECMWF10) and South Island (ECMWF7) shelves is significant throughout the weather band, and they are maximally coherent at ω_2 ($\gamma^2 = 0.88$). ECMWF10 is also significantly coherent with Hokitika and Westport, but only in the ω_2 frequency band ($\gamma^2 > 0.75$). Coherence estimates between the through-strait wind and the alongshore component of the winds at Westport or Hokitika are low ($\gamma^2 < 0.42$), although the through-strait wind is marginally coherent with the alongshore component of ECMWF7 at ω_2 only ($\gamma^2 = 0.58$). Thus,

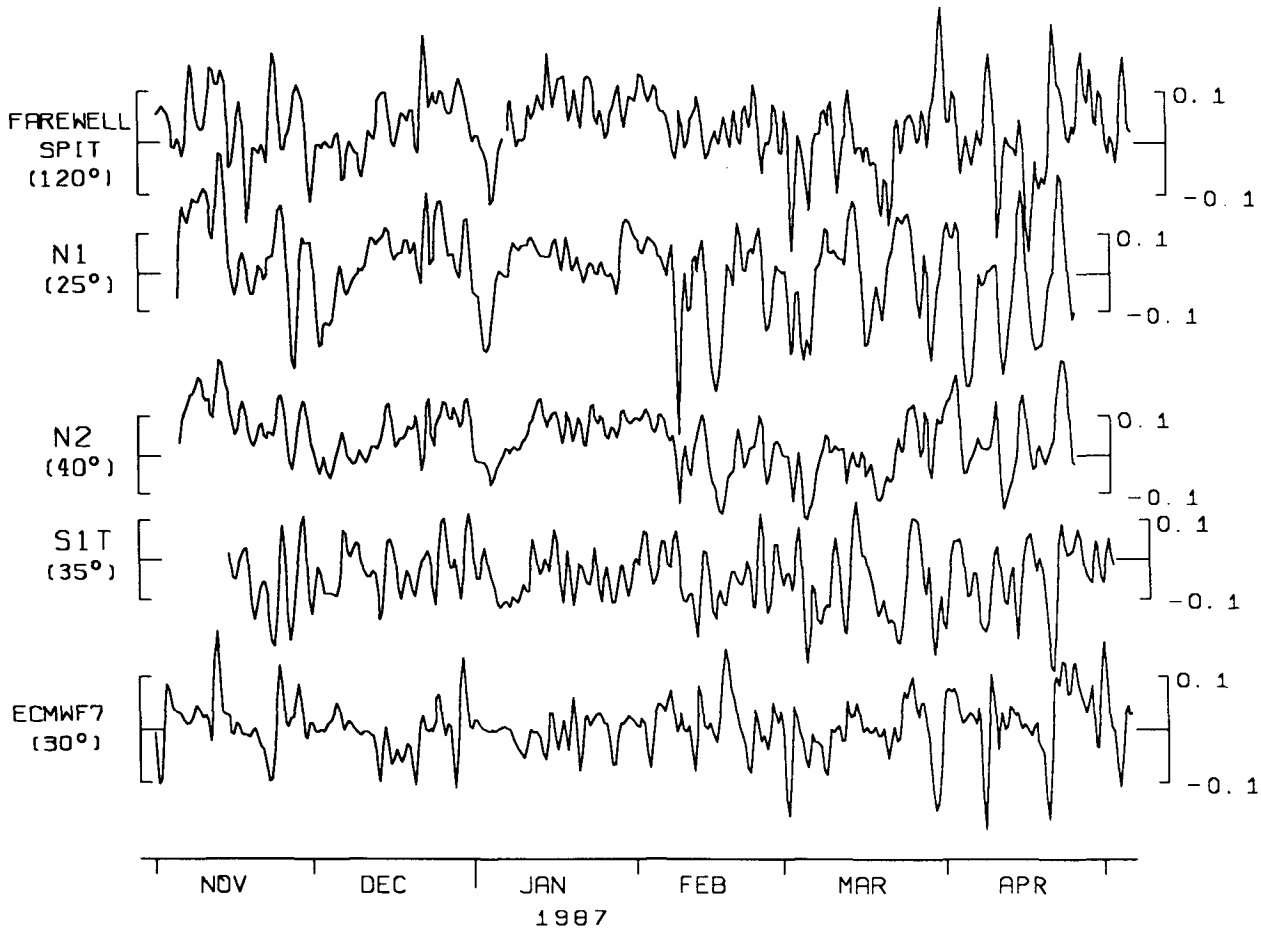

FIG. 6. Low-pass filtered time series of through-strait windstress, alongshore currents at N1, N2 and S1T and alongshore west coast windstress. Units are N m^{-2} and m s^{-1}.

it seems that, for the duration of this experiment at least, these two regions (over Cook Strait and along the west coast) of wind forcing can be considered to act essentially independently so that their contributions to the current variance should be clearly distinguishable except perhaps at ω_2.

The autospectra of wind stress in the direction of the major axis of each time series (Fig. 8) indicate the likely energy source of the three current spectra peaks. The Cook Strait winds feature spectral peaks at ω_1 and ω_3, while the west coast winds feature peaks at ω_2 only. We do not suggest that these peaks in the unsmoothed autospectra are "true" peaks in the usual sense. Instead, the significance of the peaks in the wind spectra is that they coincide with the peaks identified in the current spectra, suggesting that a causal relationship exists. The

TABLE 2. Details of the EOF analysis of the currents. Coherence estimates (γ^2 with EOF 1) are obtained by band averaging spectral and cross-spectral estimates using the Tukey window with a half-amplitude width of five spectral estimates. The through-strait wind is from Farewell Spit and the alongshore wind is from Hokitika.

Frequency band	Current variance described by EOF 1		Currents							Wind		Sea level (Port Taranaki)
	$m^2 s^{-1}$	% total	N1	N2	N3T	N3B	C3	S1T	S1B	Through-strait	Along-shore	
ω_1	.092	78	.97	.89	.05	.06	.13	.81	.71	.72	.19	.01
ω_2	.059	81	.95	.74	.04	.27	.17	.84	.78	.17	.32	.56
ω_3	.091	90	.95	.94	.58	.49	.47	.85	.80	.75	.36	.37

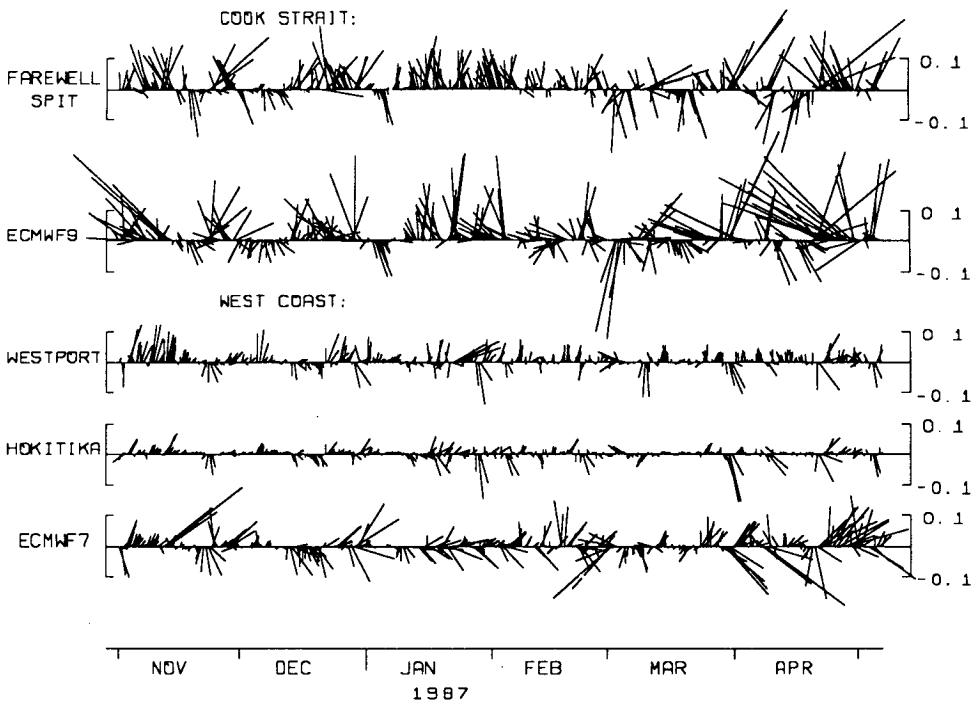

FIG. 7. Time series of the low-passed windstress vectors, plotted so that winds aligned with the principal axis of each time series (see Table 1) are drawn as vectors pointing up the page. Units are N m^{-2}.

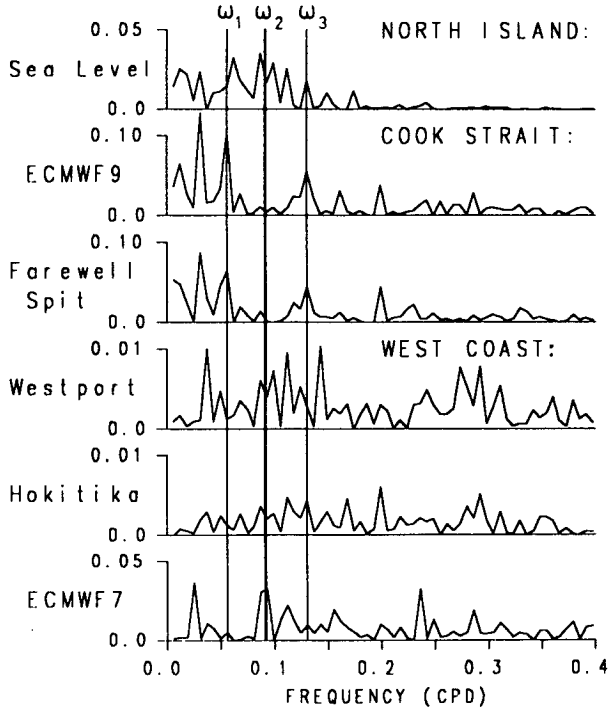

FIG. 8. Unsmoothed energy-preserving autospectra of sea level at Port Taranaki and windstress in the direction of the principal axis of each time series. Units are m^2 s for the sea level and N^2 m^{-4} s for the windstress. Only data from the same period as the currents (161 records) are used.

autospectrum is used here only to the extent that a series of events common to two time series will produce similar spectral signatures.

d. Comparisons between wind and current data

The correlation between the through-strait windstress and alongshore currents at N1 is evident from a visual comparison of the two time series (Fig. 6). For the duration of the deployment it can be seen that northeast (longshore) velocities at N1 occur soon after the wind blows southeastward through the strait. When the data are band-pass (2–25 d) filtered the correlation coefficient squared between the time series of the through-strait windstress and the current at N1 (N2) has a maximum value of 0.27 (0.38) when the windstress is lagged by 1.0 (1.0) d. If we further restrict the passed band to spectral components at periods of 25–6 d, R^2 between the Cook Strait wind and N1 (N2) increases to 0.52 (0.60) when the wind is lagged by 0.5 (1.0) d.

The band-passed (6–25 d) alongshore current at S1T was shown in section 3b to be strongly correlated with currents at the northern line. It is also significantly correlated with the alongshore west coast wind (ECMWF7) with an R^2 of 0.36 when S1T lags the wind by 1.0 d. The west coast wind, however, is only marginally correlated with currents at N1 (N2) for which R^2 is 0.08 (0.14). The alongshore wind may

explain the change with time in the values of R^2 between currents at S1T and the northern line discussed in section 3b. In Fig.6 it is evident that the high correlation between the currents during the last two months of the deployment occurs because the alongshore wind was acting on the currents at S1T to reinforce the current signal propagating from the northern line. For the rest of the deployment, however, the two forcing mechanisms do not reinforce each other, resulting in a lower correlation coefficient between currents in the north and south. With the inclusion of the west coast alongshore wind (ECMWF7) lagged by 1.0 d in a multiple regression model of the band-pass (6–25 d) filtered current at S1T, the value of R^2 is increased to 0.73 from the R^2 (0.56) obtained using only the currents at N2 lagged by 1.5 d.

The relation between the observed weather band currents and winds is readily apparent from the coherence of the various winds with the first current EOF. Estimates of γ^2 are listed in Table 2. In the frequency bands ω_1 and ω_3, only the Cook Strait windstress is significantly coherent with the first current EOF, which is consistent with the location of the energy peaks of these time series. The cospectral phase estimates indicate that the current at N1 leads the wind at Farewell Spit by 23 ± 13° at ω_1 but lags it at ω_3 by 25 ± 13°. We will attempt to explain the apparent lead at ω_1 in Section 5b.

The low level of coherence in the ω_2 frequency band of the first EOF with either of the windstress time series arises from the low coherence between the currents at N1 and N2 (which largely define this EOF) with either the through-strait wind ($\gamma^2 = 0.2$) or any of the alongshore west coast winds ($\gamma^2 \sim 0.4$ with Hokitika, Westport, ECMWF7 and ECMWF10). The current at S1, however, is significantly coherent at ω_2 with all of the alongshore west coast winds ($\gamma^2 \sim 0.67$) and also with the current at N1 ($\gamma^2 = 0.68$). Thus, it appears that currents at the southern mooring in the ω_2 frequency band are partially due to the South Island alongshore windstress as well as being due to energy propagating along the coast from the northern line. The source of the weak ω_2 signal at the northern line, however, is less obvious.

e. *Sea level*

Weather band fluctuations in the barometrically corrected sea level at Port Taranaki, 40 km north of Cook Strait, are generally less than 15 cm (not shown) and are coherent ($\gamma^2 = 0.89$ at ω_2) with the alongshore, geostrophic windstress ECMWF10 (off North Island), particularly in the frequency band ω_2. The only significant coherence between the sea level fluctuations and the first EOF of the currents occurs at ω_2 (Table 2), indicating that the energy observed on the South Island shelf at ω_1 and ω_3 does not propagate from the North Island shelf. The coherence at ω_2 suggests the possibility that energy at the northern line on the South Island shelf at this frequency originates from alongshore wind-forcing over the North Island shelf. However, the coherence is fairly marginal, suggesting either significant scattering caused by traversing the strait region or, alternatively, that the coherence may be spurious.

f. *Summary*

More than 70% (Table 2) of the nearshore alongshore current variance on the South Island west coast shelf, in the frequency bands ω_1 and ω_3, was coherent with the windstress through Cook Strait during this experiment. The currents are not coherent at these frequencies with either the North Island windstress or sea level variability so we conclude that the currents are driven by wind forcing in the strait. Wind forcing along the South Island at ω_1 and ω_3 is comparatively weak so the high coherence at these frequencies between currents at the northern line and those at the southern mooring suggests that CTWs propagate freely along the coast, despite the large alongshore changes in topography.

In the frequency band ω_2, however, the South Island alongshore windstress does appear to generate identifiable alongshore currents, particularly in the southern region. Unfortunately, the present dataset is insufficient for a detailed examination to be made in terms of locally wind-driven CTWs. One problem is that the cross-shelf structure is unknown at S1, the only location where there is significant coherence with the alongshore wind. Other obstacles include the imprecise knowledge of the winds over the coastal waters, the rapid alongshore changes in the shelf profile, and the uncertainty of the amount of energy entering the region from the North Island shelf.

For the remainder of this paper we shall therefore focus our attention on the relation between the dominant current response in the frequency bands ω_1 and ω_3, and the Cook Strait windstress. In section 5, we will compare the observations at ω_1 and ω_3 with theories of CTW generation by a coastal flux, but first we shall consider the structure of the free CTW modes for the South Island west coast shelf.

4. Free CTW mode structures

We have calculated the phase speeds and cross-shelf velocity structures of the CTW modes of the South Island west coast shelf using a computer program developed by Wilkin (1987) called *ctweig*. This program is functionally similar to *bigload*, of Brink and Chapman (1987) in that it assumes alongshore uniformity in the shelf profile and numerically solves the linearised, inviscid, hydrostatic Boussinesq equations with arbitrary across-shelf bottom topography and realistic

$N^2(z)$ profile. *Ctweig* differs from *bigload* chiefly in that vertical resolution is achieved with Chebyshev polynomials rather than by finite differencing. *Ctweig* uses a solid wall for its offshore boundary and cannot solve for the barotropic Kelvin wave as it does not have a free surface boundary condition option. CTW modal structures and phase speeds were calculated at each of the frequencies ω_1 and ω_3, once using the November N^2 profile and again using the April N^2 profile. The program was run with a grid of 201 elements in the horizontal and 18 vertical modes. For the northern line the ocean depth is taken to be 750 m and the offshore wall is placed 600 km from the coast so that two thirds of the computational domain is over a flat-bottom ocean.

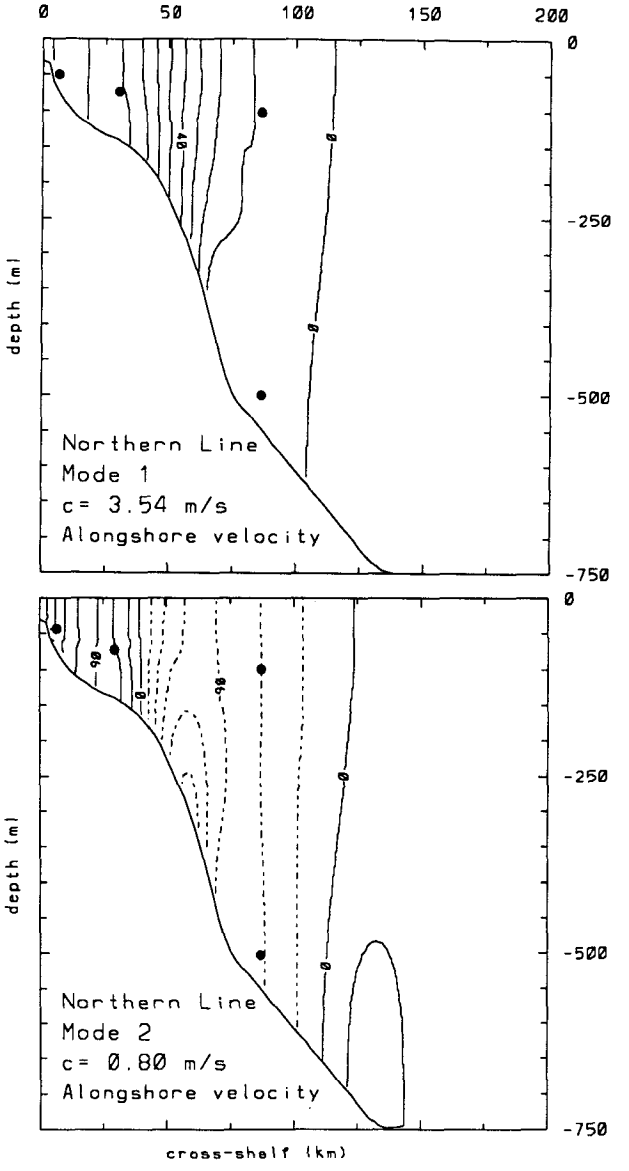

FIG. 9. The alongshore velocity structure of CTW modes 1 and 2 at the northern line. Contour values (when scaled by 10^{-7}) correspond to the alongshore velocity (m s^{-1}) for unit energy flux (W) for each mode. Negative contours are dashed. The location of each current meter is indicated by a solid dot.

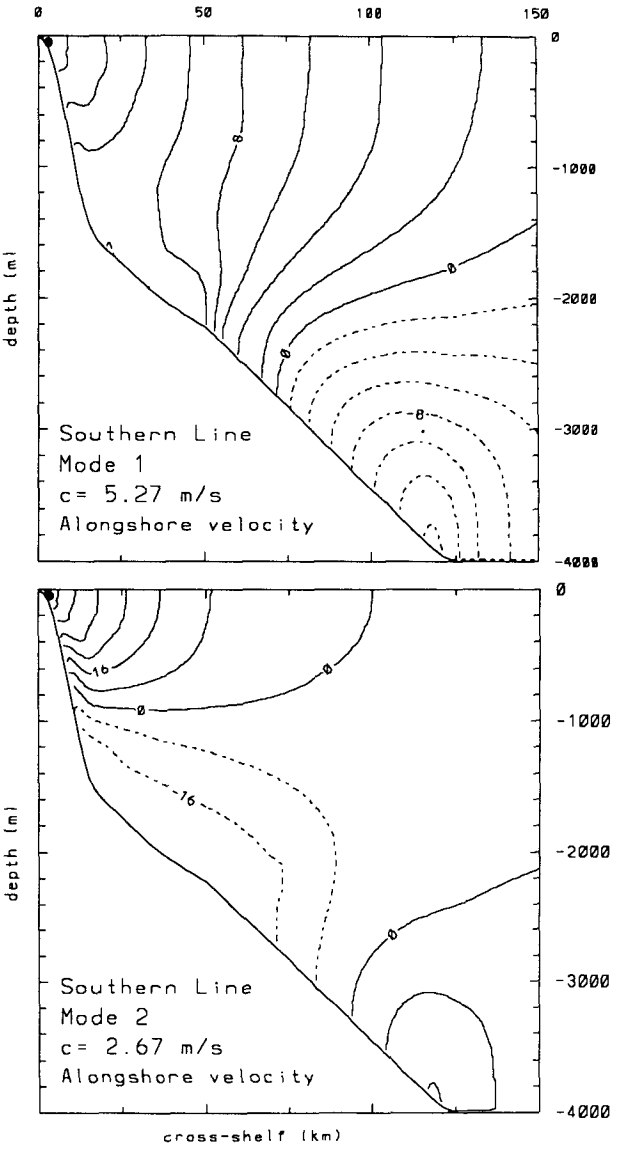

FIG. 10. As for Fig. 9 but at the southern mooring. Note the scales for offshore distance and depth are different to those used for Fig. 9.

The alongshore velocity structures of the theoretical CTW modes 1 and 2 for the northern line are almost completely barotropic, as shown in Fig. 9, despite the large value of N_{max} because the shelf gradient is small; the Burger number, $N_{max}h_x f^{-1}$, for the northern line is 0.7, where h_x is the average gradient of the shelf and slope and f is the Coriolis parameter. In comparison, the CTW modes for the shelf profile at the southern mooring (Big Bay) are highly baroclinic (Fig. 10) as the shelf is narrow and steep, with a corresponding

TABLE 3. Theoretical statistics for CTWs at the northern line: frequency, mode number, phase speed, wavelength (λ), friction coefficient (a_{nn}), frictional decay length (L_f), given $E_0^{1/2} = 0.08$, and the expected phase difference ($\theta_j(\omega)$) between the northern line and the center of Cook Strait ($\Delta y = 140$ km) of the jth mode.

Frequency (cpd)	Mode	Phase speed (m s^{-1})	λ (km)	a_{nn} (10^{-5} m^{-1})	L_f (km)	θ_j (°)
0.055	1	3.6	5655	0.258	4800	9
	2	0.94	1477	1.1	1100	34
	3	0.45	707	13.8	90	—
0.13	1	3.5	2326	0.27	4600	22
	2	0.81	538	1.2	1040	94
	3	0.44	292	32.6	40	—

Burger number of 6. We will return in section 6 to the question of how energy can propagate along the South Island west coast when the free modes are so different from one region to the next.

The phase speeds for the first three modes at the northern line (Table 3) are not greatly affected by the difference in the April and November N^2 profiles, with changes in the phase speed being less than 5% for mode 1 and less than 20% for mode 2 (the higher phase speeds corresponding to larger maximum N^2). The modal structures are also only weakly dependent on frequency and the choice of $N^2(z)$ so the main features are adequately described in Fig. 9. The alongshore velocity amplitudes m_j of modes 1 and 2 (given unit velocity at the coast) at the current meter locations on the northern line are listed in Table 4 and are used in the modal decomposition in section 5. Note that the mode 1 amplitude at the N3 mooring is less than 12% of that at N1 and N2. Also, N1 and N2 are on the same side of the nodal line of the mode 2 alongshore velocity, with N2 being close to it.

The friction coupling coefficients a_{nn} [Brink and Allen 1978, Eq. (2.13f)] are listed in Table 3 and were obtained using Brink and Chapman's barotropic CTW program. These provide an estimate for the effect of friction at the northern line. The modal structures for the northern line calculated by the barotropic CTW program differ very little from the structures found using the baroclinic *ctweig*. The frictional time scale T_f for each mode is given in terms of the Ekman number E_0, evaluated at the coast, and phase speed of the nth CTW mode by $T_f = (c_n a_{nn} E_0^{1/2})^{-1}$ (Brink and Allen 1978). It is assumed that $E_0^{1/2}$ is small, being $\sim \delta_b / h_0$ where δ_b is the Ekman bottom boundary layer depth and h_0 is the coastal depth which we will take to be equal to 75 m because the initial bottom slope at the northern line is steep (Fig. 9). The Ekman boundary layer depth is $\delta_b = 2C_D q/f$, where C_D is a drag coefficient, f is the Coriolis parameter and q is the total rms near-bottom velocity. At N1, we estimate q to be 20 cm s^{-1}, which includes the hourly measured currents and an anticipated average wind-wave climate with a deep-water amplitude of 1 m and 10 s period (R. S. Lee, personal communication). Taking C_D as 1.5×10^{-3} and $f = 0.95 \times 10^{-4}$, then $\delta_b = 6$ m and $E_0^{1/2} = 0.08$. Using this value for $E_0^{1/2}$ the frictional time scale T_f is greater than 14 days for modes 1 and 2 but less than 2 days for mode 3. The frictional decay lengths $L_f = c_n T_f$, listed in Table 3, suggest that mode 3 is highly damped and is unlikely to be energetic even at the northern line after traveling only 140 km from the center of Cook Strait.

TABLE 4. Values of m_j(N1) used in (3) and (4).

Current meter	Mode 1	Mode 2
N1	.96	.82
N2	.82	.31
N3T	.09	−.28
N3B	.06	−.32

5. CTWs generated by a coastal flux

In this section we compare the observations with the barotropic theory of Buchwald and Kachoyan (1987) for shelf waves generated by a coastal flux. The problem has also been solved for the baroclinic case by Middleton (1988), however the BK theory was considered appropriate for this application as the shelf response on the Challenger Plateau is almost entirely barotropic.

a. *Theoretical predictions*

The BK solution assumes an exponential shelf profile, $H(x) = h_0 \exp\{2bx\}$, and a strait with vertical walls and of constant depth. The flux through the strait is assumed to be constant across the strait and oscillating only in time with a cyclic frequency ω, so that $U(y, t) = U_0 \sin(2\pi\omega t)$. The downstream (in terms of CTW propagation) response over the shelf to this forcing is found to be a sum of free CTW modes with the same frequency as the forcing and zero phase at the center of the strait. The amplitude at the coast of

the alongshore velocity associated with each mode is given by

$$v_j|_{x=0} = 2\mu_j\alpha_j U_0 \sin(k_j d)/k_j, \qquad (2)$$

where k_j is the wavenumber of the free CTW of frequency ω with group velocity in the direction of the phase speed, d is half the strait width, μ_j satisfies $\tan(\mu_j) = -\mu_j/(b + |k|)$ and α_j is a parameter dependent on μ_j, the shelf profile and dispersion relation [see BK equations (3.19) and (4.6)]. The notation used here is that of BK except that their superscript which indicates that these parameters are associated with the long wavelength CTW is omitted and we use μ_j to denote BK's m_j. The sinc function dependence of the response gives almost equal amplitude to any mode having wavelength greater than twice the width of the strait, so straits with widths O(100 km) may excite CTWs of high mode number (at least locally) when subject to weather-band forcing.

The shelf profile at the western opening of Cook Strait is only constant across two-thirds of the strait opening due to the shoaling onto the northern side of the Challenger Plateau. We shall, however, assume a constant shelf profile across the opening and over the Challenger Plateau the profile can be adequately described by an exponential, where $h_0 = 75$ m is the depth at the coast and $b = 1.15 \times 10^{-5}$ m^{-1}. For the first three CTW modes, there is less than an 8% difference between the wavenumbers calculated for an exponential shelf in a barotropic ocean and those calculated using real stratification and bottom topography. The effect that shoaling of the bottom topography onto the Challenger Plateau has on the amplitudes of the CTW modes generated by the strait is not known. Presumably some energy could propagate northwestward along the edge of the plateau reducing the amplitudes of the modes trapped to the coast, although, we assume that this effect is small.

Cook Strait has a maximum depth of 100 m and resembles a triangle in cross section more than a square, but to fit the theory of BK, we have modeled it as having vertical sides of depth 75 m and width 140 km. Using these values, the amplitudes at the coast of the alongshore velocity associated with the first three modes, normalized by the amplitude of the depth-averaged, through-strait velocity U_0, are shown in Table 5. The model predicts currents at the coast due to mode 2 to be slightly greater than those due to mode 1 at both ω_1 and ω_3.

b. *Preliminary comparisons between theory and observations*

The implications of the BK theory can now be cast in terms of some of the observable quantities at the northern line. The mode 3 CTW on the shelf over the Challenger Plateau has a very short frictional decay length so we assume that only modes 1 and 2 would be observable at the northern line. The (complex) alongshore velocity **V** at mooring Nl, obtained by the superposition of two CTW modes generated by the flux through Cook Strait, is given by

$$\mathbf{V}(\mathrm{N}l, \omega) = \sum_{j=1}^{2} v_j(\omega)|_{x=0} m_j(\mathrm{N}l) e^{i\theta_j(\omega)}. \qquad (3)$$

The $m_j(\mathrm{N}l)$ are the cross-shelf structure functions, evaluated at Nl (Table 4), of the jth CTW mode, as determined using *ctweig* and normalized such that the velocity amplitude of each mode at the coast is unity. The phase $\theta_j(\omega) = k_j \Delta y$ due to propagation alongshore of the jth mode from the center of the strait ($\Delta y = 140$ km) is listed in Table 3. The unit imaginary number is denoted by i. Strictly speaking, the $m_j(\mathrm{N}l)$ are dependent on frequency and stratification, however, the effect of this dependence is comparable to the accuracy obtainable in numerically determining the modal structure. Therefore, the results using only one matrix of $m_j(\mathrm{N}l)$ (associated with CTWs of frequency ω_3 and using the April N^2 profile) are shown.

The magnitude of $\mathbf{V}(\mathrm{N}l, \omega)$ is proportional to the (unknown) through-strait flux U_0. One of the critical observable quantities is, therefore, $|\mathbf{V}(\mathrm{N2}, \omega)|\,/\,|\mathbf{V}(\mathrm{N1}, \omega)|$, which is 0.60 (0.64) at frequency ω_1 (ω_3). We find that this ratio is close to the observed cospectral gain $|\mathbf{H}_{\mathrm{N2/N1}}|$, which is 0.58 ± 0.08 (Fig. 5b), and even closer to the gain obtained using the first EOF ($|\mathrm{E1}_{\mathrm{N2}}|/|\mathrm{E1}_{\mathrm{N1}}|$), which is 0.60 (0.62) at ω_1 (ω_3).

The other critical observable quantity is the cross-shelf phase difference between currents at N1 and N2. The theoretical phase difference $\theta^t_{\mathrm{N2/N1}} = \arg[\mathbf{V}(\mathrm{N2}, \omega)/\mathbf{V}(\mathrm{N1}, \omega)]$ is −5° (−16°) at ω_1 (ω_3), which indicates that N2 should lead N1 because the mode 2 contribution reduces faster with distance offshore. However, the observed cospectral phase $\theta^c_{\mathrm{N2/N1}} = \arg(\mathbf{H}_{\mathrm{N2/N1}})$ is 29 ± 7° (21 ± 7°) at ω_1 (ω_3) (Fig. 5b), indicating that currents at N2 lag those at N1. What could account for this (nearly) frequency independent $[\theta^c_{\mathrm{N2/N1}} - \theta^t_{\mathrm{N2/N1}} = 34°\ (37°)$ at ω_1 (ω_3)] nearshore phase lead?

A nearshore phase lead caused by friction is commonly predicted in the literature for the case of a current forced by an alongshore windstress. Observations of nearshore phase leads have also generally been for the locally wind-forced case, rather than for the less commonly observed freely propagating waves. Brink et al. (1978), however, observed that remotely forced currents at a nearshore mooring (in 40 m on the shelf of Peru) led those at an offshore mooring (in 123 m) by one day. They ascribed this phase advance to the effects of a cross-shelf gradient in the relative importance of friction. We suggest that the nearshore phase lead we observe at the northern line is also due to friction. The weak dependence on frequency of $\theta^c_{\mathrm{N2/N1}}$

$-\theta^{t}_{N2/N1}$ is consistent with the conclusion of Brink and Allen (1978) who showed that the nearshore frictional phase lead is only slightly dependent on frequency through its dependence on the CTW phase speed and structure.

A nearshore frictional phase advance could also account for the apparent lead at ω_1 of the current at N1 with respect to the wind at Farewell Spit. The theoretical (frictionless) phase difference $\theta^{t}_{N1/\tau}$ between the currents at N1 and the through-strait windstress can be expressed as $\theta^{t}_{N1/\tau} = \arg[\mathbf{V}(N1, \omega)] + \theta_r$ where $\arg[\mathbf{V}(N1, \omega)]$ (22° at ω_1 and 59° at ω_3) is the phase due to propagation of the two modes from the strait and θ_r is the phase associated with the response time of the wind-driven flux through Cook Strait. The response time of Cook Strait is unknown, so we use the response time of Bass Strait which Morrow et al. (1990) estimated to be 6 h, giving $\theta_r = 5°$ (12°) at ω_1 (ω_3). Thus, we obtain $\theta^{t}_{N1/\tau}$ to be 27° (71°) at ω_1 (ω_3). The observed cospectral phase $\theta^{c}_{N1/\tau}$, however, is $-23 \pm 13°$ ($25 \pm 13°$) at ω_1 (ω_3). Assuming that the difference between the theoretical and observed phases is largely due to friction we obtain estimates of the frictional phase lead at N1 ($\theta^{f}_{N1} = \theta^{t}_{N1/\tau} - \theta^{c}_{N1/\tau}$) to be 50° (46°) at ω_1 (ω_3). The frictional phase advance at N2 can be obtained by subtracting the previously determined advance of N1 relative to N2 ($\theta^{c}_{N2/N1} - \theta^{t}_{N2/N1}$) from θ^{f}_{N1}, yielding $\theta^{f}_{N2} = 16°$ (9°) at ω_1 (ω_3).

The predicted $v_j|_{x=0}$ are greater than the (unmeasured) through-strait velocity U_0 by factors of 1.9 or greater (Table 5). Thus, the amplitude of the current through the western opening of Cook Strait can be estimated to be approximately one-half the amplitude of that observed at N1. The standard deviation of the alongshore current at N1 is 11.6 cm s^{-1}, so the standard deviation of the through-strait current will be ~6 cm s^{-1}. Cook Strait narrows on the eastern side to a width of 22 km (approximately one-sixth of the width at the western side), but it also deepens to an average depth of 250 m, so that the minimum cross-sectional area of the strait is about one-half of that at the western opening. Thus, the maximum expected value of the standard deviation of currents in Cook Strait is a plausible ~12 cm s^{-1}. Due to instrument losses, however, we have no direct measurements of low frequency currents in the strait to verify this expectation.

TABLE 5. Alongshore velocity amplitudes, $v_j|_{x=0}/U_0$, and the ratio of the mode 1 and mode 2 values (v_2/v_1).

Frequency (cpd)	Mode 1	Mode 2	Mode 3	v_2/v_1
0.055	1.9	2.5	2.5	1.3
0.13	2.0	2.4	0.6	1.2

c. Modal decomposition

The theoretical CTW modes at the northern line are highly barotropic, so the two current meters on mooring N3 should provide no more information about the CTW modes than does one meter. We therefore have the equivalent of only three measurement locations to use for mode-fitting at the northern line. To avoid "over-fitting" (Hsieh 1982) and because mode 3 is so heavily damped, we have chosen to fit the observations to only two modes.

The current recorded by N3T is dominated by non-CTW signals of very low frequency and hence cannot be included in a fit to CTW modal structure. The modal decomposition is therefore performed as a least squares fit in the frequency domain to only three locations, such that:

$$\begin{bmatrix} m_1(N1) & m_2(N1) \\ m_1(N2) & m_2(N2) \\ m_1(N3) & m_2(N3) \end{bmatrix} \times \begin{bmatrix} \mathbf{a}_1 \\ \mathbf{a}_2 \end{bmatrix} = \begin{bmatrix} \mathbf{v}_{N1} \\ \mathbf{v}_{N2} \\ \mathbf{v}_{N3} \end{bmatrix} - \begin{bmatrix} \mathbf{r}_{N1} \\ \mathbf{r}_{N2} \\ \mathbf{r}_{N3} \end{bmatrix} \quad (4)$$

where $\mathbf{a}_j(\omega)$ is the (unknown) complex amplitude of the alongshore velocity associated with the jth mode CTW at the coast (for comparison with BK's $v_j|_{x=0}$), $\mathbf{r}_{Nl}(\omega)$ is the residual of the fit to $\mathbf{v}_{Nl}(\omega)$, which is the complex Fourier coefficient of the alongshore velocity at location Nl.

The small number of instruments and the low energy at the outer mooring combined with the largely rectilinear currents render the modal decomposition a fairly simple operation; effectively, a fit of modes 1 and 2 to the ratio of current amplitudes at N2 to N1. This ratio is ~0.9 for mode 1 and ~0.4 for mode 2, while the observed ratio is ~0.6. N2 is near the zero crossing for mode 2 so the fit is potentially unstable to small variations in the modal structure. This instability is overcome by the added restriction of low energy at the outer mooring, which limits the amplitude of mode 2. Stability, however, does not necessarily imply the presence of CTW modes, and with this simple fit, any nearshore intensified current variability can be described with two CTW modes. The modal decomposition, therefore, cannot strictly be used to infer the presence of CTWs, but once we accept that the currents are due largely to CTWs, the modal decomposition can be used to determine their relative amplitudes.

The theory of BK predicts that CTWs will be generated by a coastal flux and the results of the spectral analysis in section 3 show high coherence between the Cook Strait winds and currents at both the northern line and the southern mooring. We therefore assume that there are propagating CTWs on this shelf, which are generated by the wind through Cook Strait. Thus, rather than fitting the modes to the alongshore velocity data, we shall use only the velocity which is coherent with the windstress at Farewell Spit, $\mathbf{v}^{\tau}_{Nl}$, with the property that

$$\mathbf{v}^{\tau}_{Nl}(\omega) = \tau(\omega)\mathbf{H}_{Nl/\tau}(\omega), \quad (5)$$

where $\tau(\omega)$ is the Fourier coefficient of the wind at Farewell Spit at frequency ω. The modal amplitudes obtained from the modal fit using the $\mathbf{v}^{\tau}_{Nl}$ shall be referred to by $\mathbf{a}_j{}^{\tau}$.

The percentage variance for all three current meter time series at each frequency which is not accounted for by the decomposition into CTW modes is given by

$$\epsilon = \frac{\sum_{l=1}^{3} \mathbf{r}^{*}_{Nl}\mathbf{r}_{Nl}}{\sum_{l=1}^{3} (\mathbf{v}^{\tau}_{Nl})^{*}\mathbf{v}^{\tau}_{Nl}}. \quad (6)$$

At ω_1 and ω_3, ϵ is 2% and is never higher than 5% for other frequencies in the weather band.

The magnitude of the (complex) modal amplitudes, $a_j{}^{\tau}(\omega)$ are shown in Fig. 11. The ratio $a_2{}^{\tau}(\omega)/a_1{}^{\tau}(\omega)$ is 0.9 at ω_3 and compares favourably with the predicted ratio of 1.2 using the theory of BK. At ω_1, the ratio is 0.7 which, although not as large as the predicted ratio of 1.3, still represents a large proportion of energy due to mode 2. As previously mentioned, almost all of the current fluctuations contributing to the signal at ω_3 occurred in the last two and a half months of the deployment. A modal fit in the same manner, but using data from this period only, gives a modal amplitude ratio $\mathbf{a}_2{}^{\tau}/\mathbf{a}_1{}^{\tau}$ of 1.0 at ω_3, slightly closer to the predicted ratio.

For comparison, the modal amplitudes $\mathbf{a}_j(\omega)$ [determined using $\mathbf{v}_{Nl}(\omega)$ in (4) rather than the $\mathbf{v}^{\tau}_{Nl}(\omega)$] are shown in Fig. 11b. The amplitudes of mode 1 at ω_1 and both modes at ω_3 are increased by up to 20%,

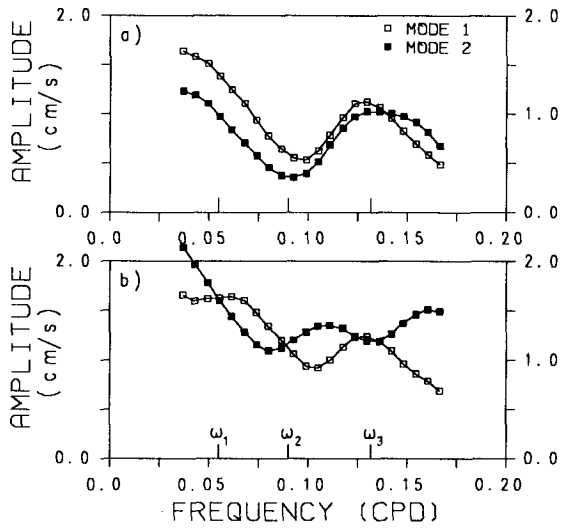

FIG. 11. The amplitudes $|a_j{}^{\tau}(\omega)|$ and $|a_j(\omega)|$ of CTW modes 1 and 2 at the northern line determined by a model fit to (a) the $\mathbf{v}^{\tau}_{Nl}$ and (b) the $\mathbf{v}_{Nl}$ at N1, N2 and N3B.

while at ω_1 the mode 2 amplitude is increased by 60%. The time series $a_1(t)$ and $a_2(t)$ obtained from the inverse Fourier transform of the coefficients $\mathbf{a}_1(\omega)$ and $\mathbf{a}_2(\omega)$ and also the sum of these two time series are all significantly coherent (Fig. 12) with the through-strait wind at both ω_1 and ω_3 except for mode 2 at ω_1.

d. The effect of a cross-shelf phase gradient

Phase differences between the $\mathbf{a}_j(\omega)$ and the through-strait wind (Fig. 12) show that mode 2 leads the wind at ω_1, which would not be the case if, as we are proposing, the CTWs are generated by the strait. We are, however, fitting frictionless modes to observations which are affected by friction (as discussed in section 5b). To account for the effects of friction we have experimented with retarding the Fourier coefficients $\mathbf{v}_{N1}(\omega)$ and $\mathbf{v}_{N2}(\omega)$, which are input to the modal de composition by the estimated frictional phase lead at each location θ^{f}_{N1} and θ^{f}_{N2} (44° and 10°). These phase lead estimates are a reevaluation of those obtained in section 5b, using the amplitudes of the modes $\mathbf{a}_j{}^{\tau}$ from the modal decomposition rather than the predicted modal amplitudes. We find that the amplitudes of the fitted modes remain largely unaltered and the phase of mode 1 is retarded by ~10°. However, as shown in Fig. 12c, the phase of mode 2, which is sensitive to the relative phase advance between N1 and N2, is retarded by more than 90° so that mode 2 lags the wind by 38 ± 26° (85 ± 16°) at ω_1 (ω_3), in greater accord with the theoretical phase of mode 2 ($\theta_j(\omega) + \theta_r$) which is 39° (106°) at ω_1 (ω_3). The direction and magnitude of the phase shift of mode 2, caused by retarding the input Fourier coefficients to the modal fit, suggest that it is possible for a frictional phase lead to account for the apparent inconsistencies between the observed phase at N1 and that predicted by inviscid theory, although we stress that these calculations are only indicative.

6. Comparison of observations at the northern line with those at the southern mooring

The coherence between currents at the northern and southern lines, particularly at ω_1 and ω_3, at which frequencies the west coast wind is neither energetic nor coherent with the currents, suggests that the energy observed at the northern line propagates in some form along the coast to the southern mooring. The considerable difference in the across-shelf depth profiles and associated CTW modal structures at the two locations indicates that the barotropic CTWs on the Challenger Plateau must undergo major adjustments to their across-shelf structures in order to exist as the highly baroclinic CTWs calculated for the much steeper shelf in the southern regions of the west coast.

The loss of most of the data from the central line severely limits what can be concluded concerning the

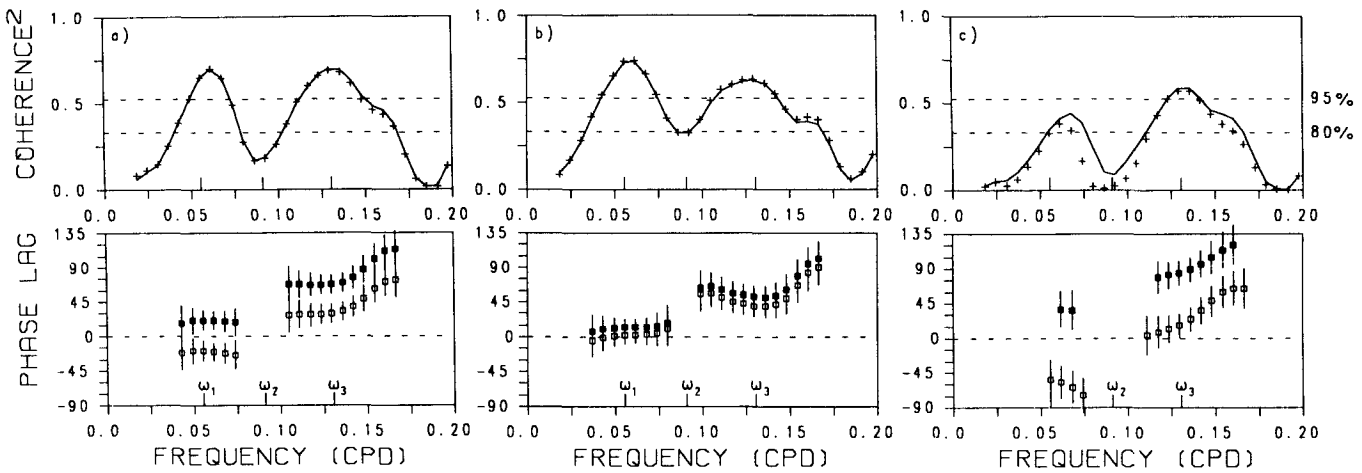

FIG. 12. Estimates of the coherence squared and cospectral phase between the Cook Strait windstress and (a) $a_1 + a_2$, (b) a_1 and (c) a_2, where a_1 and a_2 are the times series of the fitted CTW modes 1 and 2. Two sets of estimates are shown on each plot, one obtained from (4) using the $v_{Nl}(\omega)$ and the other obtained after phase shifting the $v_{Nl}(\omega)$ to account for friction. The latter are plotted as +'s and solid boxes. A positive phase lag indicates that the CTW mode time series lags the wind.

alongshore evolution of CTWs. However, it is of interest to compare the current amplitudes and phases at the southern mooring with those one might expect if the CTW modes 1 and 2 propagate from the northern line without loss of energy, adjusting their structure and wavelength with the shelf profile. We will call this the zero-scattering scenario.

The amplitude of the velocity associated with each mode at S1T relative to that at N1 for the zero-scattering scenario is simply $\hat{m}_j(\mathrm{S1T})/\hat{m}_j(\mathrm{N1})$, where the caret indicates that the CTW across-shelf structure function m_j (calculated using the local shelf profile) has been renormalized so that each mode has unit alongshore energy flux (instead of unit coastal velocity). We evaluate this ratio for mode 1 (2) to be 0.2 (0.3) at ω_1 and 0.2 (0.4) at ω_3. In comparison, the observed velocity ratio obtained from the first EOF $|\mathrm{E1_{S1T}}|/|\mathrm{E1_{N1}}|$ is 0.54 at ω_1 and 0.63 at ω_3, roughly twice the value possible for the zero-scattering scenario.

These higher observed current amplitudes at S1 suggest that the energy flux of the barotropic CTWs on the Challenger Plateau remains in the shallower regions of the shelf as the shelf deepens, perhaps through scattering into more closely coastally trapped modes. This is as anticipated by the (barotropic) theory of Johnson (1989) who considers the scattering induced when the shelf profile changes from one exponential to another of a different slope. The amplitudes of the transmitted modes are proportional to $(n^2 - \beta^2 m^2)^{-1}$ where β is the ratio of the logarithmic slopes and n and m are the transmitted and incident mode numbers, respectively. In the present case where β, the ratio of the shelf slopes at the southern and northern lines, is $\sim$2.7, scattering into modes 2 through 6 is predicted. Further investigation into the rate at which energy is scattered into the higher modes and dissipated is beyond the scope of this study. However, we note that CTW modes on the shelf between the northern and southern lines will have longer frictional length scales than those obtained for the northern line CTWs (Table 3) as the phase speeds of modes in the southern regions are considerably higher.

The propagational phase lags for the zero-scattering case may be determined by dividing the shelf into many sections (we have used 10, each about 50 km in length), and choosing a representative shelf profile for each section. The phase speeds for modes 1 and 2 on each section are found using *ctweig* and converted to a time lag across the section. The sum of the time lags along the coast gives total lags between N1 and S1 of 0.7 d for mode 1 and 2.4 d for mode 2. These time lags correspond to phase differences for modes 1 and 2 of 14° and 48° at ω_1 and 33° and 112° at ω_3. To compare these phase differences with those observed, estimates of the relative importance of the two CTW modes at S1 are required. Assuming that at N1 the ratio of the amplitudes of modes 1 and 2 is approximately 1.0, we find that the corresponding zero-scattering time lags are 1.7 d at ω_1 and 1.9 d at ω_3. These estimates are obtained using (3) but with the substitution of $\hat{m}_j(\mathrm{S1T})/\hat{m}_j(\mathrm{N1})$ for $v_j|_{x=0} m_j$ and using the propagational phase difference of each mode between the northern and southern lines instead of the phase difference θ_j between the strait and the northern line. The observed cospectral phase $\theta^c_{\mathrm{S1T/N1}}$ at ω_1 (see Fig. 5a) corresponds to a time lag of 2.8 d which is 1.1 d longer than the zero-scattering time lag, again suggesting the scattering of energy to higher modes. At ω_3, however, the observed time lag is 1.7 d which is within 0.2 d of the zero-scattering time lag.

The problem of quantifying the scattering effect of any particular shelf topography is considered by Wilkin and Chapman (1990). They introduce the warp factor F_w as a measure of the shelf's departure from shelf-similarity. The concept of shelf-similarity was first introduced by Hsueh (1980) and then generalized by Davis (1983) with the inclusion of short wavelength CTWs. A shelf that varies alongshore yet remains shelf-similar will not scatter CTWs. Once off the Challenger Plateau, the warp factor for the west coast shelf of South Island is ~0.4. This is an order of magnitude greater than that of the shelves considered in the numerical experiments of Wilkin and Chapman, where F_w ranged from zero (no scattering) to 0.04, for which case up to 20% of the incident energy was found to be scattered. In addition, the large canyons that cut deeply into the continental shelf, particularly in the southern region, may lead to significant energy loss or scattering (Wang 1980), and at this stage it is not obvious what their effect on the currents observed at S1 would be.

It thus appears that the zero-scattering scenario is unlikely to be appropriate, from both theoretical and observational grounds. An important outcome of the present experiment is the observation that energy does manage to traverse a region of substantial scattering without being entirely dissipated in the process, resulting in currents at S1 being substantially stronger than they would be if energy remained entirely in the first two CTW modes.

7. Summary and concluding remarks

For the duration of this experiment most of the weather-band current variance on the northern shelf is coherent with the through-strait windstress and not coherent with either alongshore winds over the shelf or the sea level measured at North Island. With no other energy source apparent it seems reasonable to conclude that CTW modes on the west coast shelf are generated by the wind-driven flux through Cook Strait. A fit of CTW modal structures to the currents at the northern line of current meters indicates that both modes 1 and 2 contribute nearly equally to the nearshore current, in agreement with the theory of Buchwald and Kachoyan (1987). Farther offshore, on the Challenger Plateau, surface intensified motions are observed, which are of larger amplitude and lower frequency than can be explained in terms of CTWs.

The highly significant coherence observed between the currents at the southern mooring and those at the northern line, particularly at the frequencies $\omega_1 = 0.055$ and $\omega_3 = 0.13$ cpd at which there is little energy in the alongshore winds, indicates that the energy of the CTWs generated on the northern region of the shelf is transmitted at least 600 km to the southern mooring despite the large alongshore variations of the shelf topography. A comparison of the observed phase lags and relative amplitudes of the currents in the north and south with those expected for freely propagating, unscattered, energy conserving CTW modes suggests a considerable degree of scattering into more slowly propagating, nearshore-trapped modes.

South Island alongshore wind-forcing also contributes to the current variance observed at the southern mooring, showing up in the present dataset as a spectral peak at $\omega_2 = 0.09$ cpd. While forcing by west coast winds is therefore undoubtedly of importance it appears that during this experiment the currents generated by the flux through Cook Strait are responsible for the bulk of the variance (at periods of 6–25 d) on the South Island west coast shelf.

This result is analogous to that of ACE (Church et al. 1986a,b; Freeland et al. 1986) where CTWs were found to be generated by the flux through Bass Strait, so it is appropriate to make some comparisons. In general, the currents associated with CTWs observed off southeast Australia during ACE were a lot stronger than those measured on the New Zealand shelf during the six months of this experiment. For example, the alongshore current observations from the location in ACE closest to Bass Strait, on the Cape Howe section at 75 m depth, in 140 m of water (instrument 11/75 in ACE notation) have a standard deviation of 30 cm s^{-1} (Huyer et al. 1988). In comparison, the standard deviation of the currents at N2 at a similar depth is only 8 cm s^{-1} and at N1 in 74 m of water it is only 12 cm s^{-1}. For the CTWs on the two shelves to have equal energy flux, the ratio of alongshore velocity at N1 to that at 11/75 would be ~1.5 for both modes 1 and 2. Thus the ratio of the observed standard deviation of the alongshore velocities (0.4) implies that the CTW energy flux along the west coast shelf of South Island was only 7% of that on the NSW shelf.

An estimate of the time-averaged energy flux associated with the CTWs on the New Zealand shelf during the experiment may be made by normalizing the a_j^r of (4) so that they are a measure of energy flux rather than coastal current amplitude. The energy flux, summed over the frequency band of interest, is then

$$F = \sum_{\omega} \sum_{j=1}^{2} (\hat{\mathbf{a}}_j^r)^* \hat{\mathbf{a}}_j^r. \tag{7}$$

For the band 0.05–0.15 cpd we obtain

$$F = 2.1 \times 10^7 \text{ W},$$

one-ninth of the estimate of CTW energy flux, 1.8×10^8 W, obtained by Freeland et al. (1986) for the Cape Howe line during ACE.

The relatively low energy of these CTWs can be explained in part by the comparatively weak winds through Cook Strait compared with those through Bass Strait. The standard deviation of along-strait windstress measured by Kingfish B (an oil rig at the eastern mouth

of Bass Strait) for six months during ACE, is 0.23 N m^{-2} (Morrow et al. 1990) while that at Farewell Spit is only 0.09 N m^{-2} for the period of our deployment. In addition, the locally driven flux through Bass Strait is possibly augmented by wind-driven CTWs generated along the long stretch of wide shelf of the Great Australian Bight (Church and Freeland 1987) whereas no comparable analogue exists for Cook Strait [unless Chatham Rise (Fig. 1) proves to support topographic waves].

Finally, we note that if Cook Strait did not exist, the low frequency currents on the west coast shelf of South Island, forced only by the weak alongshore winds with phase speed in the opposite direction of free CTWs, would be even less energetic than the weak currents now observed.

Acknowledgments. This project was supported by Australian Marine Sciences and Technologies Grant 85/994, Australian Research Council Grant A88831574 and the Postgraduate Research Awards Scheme. We thank Greg Nippard and Bruce Shakespeare for the implementation of the field program, Malcolm Greig for calibrating the current data and Frank Viera for providing the computer programs to calculate the BK predictions. Finally, we thank David Griffin for helpful discussion and comments on this paper.

REFERENCES

Bendat, J. S., and A. G. Piersol, 1980: *Engineering Applications of Correlation and Spectral Analysis.* Wiley & Sons, 278–280.

Brink, K. H., and J. S. Allen, 1978: On the effect of bottom friction on barotropic motion over the continental shelf. *J. Phys. Oceanogr.*, **8,** 919–922.

——, and D. C. Chapman, 1987: Programs for computing properties of coastal-trapped waves and wind-driven motions over the continental shelf and slope, second ed. Woods Hole Oceanographic Inst. Tech. Rep. WHOI-87-24, 119 pp.

——, J. S. Allen and R. L. Smith, 1978: A study of low-frequency fluctuations near the Peru coast. *J. Phys. Oceanogr.*, **8,** 1025–1041.

Buchwald, V. T., and B. J. Kachoyan, 1987: Shelf waves generated by a coastal flux. *Aust. J. Mar. Freshwater Res.*, **38,** 429–437.

Church, J. A., and H. J. Freeland, 1987: The energy source for the coastal trapped waves in the Australian Coastal Experiment Region. *J. Phys. Oceanogr.*, **17,** 289–300.

——, —— and R. L. Smith, 1986a: Coastal-trapped waves on the east Australian continental shelf. Part I: Propagation of modes. *J. Phys. Oceanogr.*, **16,** 1929–1943.

——, N. J. White, A. J. Clarke, H. J. Freeland and R. L. Smith, 1986b: Coastal-trapped waves on the east Australian continental shelf. Part II: Model verification. *J. Phys. Oceanogr.*, **16,** 1945–1958.

Crawford, W. R., 1984: Energy flux and generation of diurnal shelf waves along Vancouver Island. *J. Phys. Oceanogr.*, **14,** 1600–1607.

——, and R. E. Thomson, 1984: Diurnal-period continental shelf waves along Vancouver Island: A comparison of observations with theoretical models. *J. Phys. Oceanogr.*, **14,** 1629–1646.

Davis, A. M. J., 1983: Shelf similar topographies for free continental shelf waves. *Geophys. Astrophys. Fluid. Dyn.*, **23,** 321–331.

Flather, R. A., 1988: A numerical model investigation of tides and diurnal-period continental shelf waves along Vancouver Island. *J. Phys. Oceanogr.*, **18,** 115–139.

Freeland, H. J., F. M. Boland, J. A. Church, A. J. Clarke, A. M. G. Forbes, A. Huyer, R. L. Smith, R. O. R. Y. Thompson and N. J. White, 1986: The Australian Coastal Experiment: A search for coastal trapped waves. *J. Phys. Oceanogr.*, **16,** 1230–1249.

Hardy, D. M., and W. W. Walton, 1978: Principal components analysis of vector wind measurements. *J. Appl. Meteor.*, **17,** 1153–1162.

Hsieh, W. W., 1982: On the detection of continental shelf waves. *J. Phys. Oceanogr.*, **12,** 414–427.

Hsueh, Y., 1980: Scattering of continental shelf waves by longshore variations in bottom topography. *J. Geophys. Res.*, **85,** 1147–1150.

Huyer, A., R. L. Smith, P. J. Stabeno, J. A. Church and N. J. White, 1988: Currents off south-eastern Australia: Results from the Australian Coastal Experiment. *Aust. J. Mar. Freshwater Res.*, **39,** 245–288.

Johnson, E. R., 1989: Connection formulae and classification of scattering regions for low-frequency shelf waves. *J. Phys. Oceanogr.*, **19,** 1301–1310.

Large, W. S., and S. Pond, 1981: Open-ocean momentum flux measurements in moderate to strong winds. *J. Phys. Oceanogr.*, **11,** 324–336.

Middleton, J. F., 1988: Long shelf waves generated by a coastal flux. *J. Geophys. Res.*, **93,** 10 724–10 730.

Morrow, R. A., P. J. Stabeno, R. L. Smith and I. S. F. Jones, 1990: Bass Strait forcing of coastal trapped waves; ACE revisited. *J. Phys. Oceanogr.*, **20,** 1528–1538.

Thompson, R. O. R. Y., 1979: Coherence significance levels. *J. Atmos. Sci.*, **36,** 2020–2021.

Wallace, J. M., and R. E. Dickinson, 1972: Empirical orthogonal representation of time series in the frequency domain. Part I: Theoretical considerations. *J. Appl. Meteor.*, **11,** 887–892.

Wang, D.-P., 1980: Diffraction of continental shelf waves by irregular alongshore geometry. *J. Phys. Oceanogr.*, **10,** 1187–1199.

Wilkin, J. L., 1987: A computer program for calculating frequencies and modal structures of free coastal-trapped waves. Woods Hole Oceanographic Institution. Tech. Rep. WHOI 87-53, 50 pp.

——, and D. C. Chapman, 1990: Scattering of coastal-trapped waves by irregularities in coastline and topography. *J. Phys. Oceanogr.*, **20,** 396–421.